# Band-Filling of Solution-Synthesized CdS Nanowires

**James Puthussery,[†] Aidong Lan,[†] Thomas H. Kosel,[‡] and Masaru Kuno[†,*]**

[†]Department of Chemistry and Biochemistry, Notre Dame Radiation Laboratory, and [‡]Department of Electrical Engineering, University of Notre Dame, Notre Dame, Indiana 46556

**ABSTRACT** The band edge optical characterization of solution-synthesized CdS nanowires (NWs) is described. Investigated wires are made through a solution—liquid–solid approach that entails the use of low-melting bimetallic catalyst particles to seed NW growth. Resulting diameters are approximately 14 nm, and lengths exceed 1 μm. Ensemble diameter distributions are ~13%, with corresponding intrawire diameter variations of ~5%. High-resolution transmission electron micrographs show that the wires are highly crystalline and have the wurtzite structure with growth along at least two directions: [0001] and [10|$$10]. Band edge emission is observed with estimated quantum yields between ~0.05% and 1%. Complementary photoluminescence excitation spectra show structure consistent with the linear absorption. Carrier cooling dynamics are subsequently examined through ensemble lifetime and transient differential absorption measurements. The former reveals unexpectedly long band edge decays that extend beyond tens of nanoseconds. The latter indicates rapid intraband carrier cooling on time scales of 300–400 fs. Subsequent recovery at the band edge contains significant Auger contributions at high intensities which are usurped by other, possibly surface-related, carrier relaxation pathways at lower intensities. Furthermore, an unusual intensity-dependent transient broadening is seen, connected with these long decays. The effect likely stems from band-filling on the basis of an analysis of observed spectral shifts and line widths.

**KEYWORDS:** CdS · nanowire · one-dimensional · solution—liquid–solid · band edge emission · transient differential absorption spectroscopy · Auger · band-filling · many body · band gap renormalization

Conventional materials science has been revolutionized by opportunities in modulating the size, structure, morphology, and chemical composition of nanoscale materials. In this regard, the properties of matter can be deliberately tuned through size- and shape-dependent effects, allowing integration of functional nanoscale materials into a wide range of applications. Key issues that remain to be addressed, however, include the development of well-defined syntheses for these nanostructures as well as a better understanding of their underlying growth mechanisms. Furthermore, detailed insights into their fundamental optical properties are needed from both basic science and applied perspectives.

Semiconductor nanostructures stand out due to the existence of quantum confinement effects, leading to size- and shape-dependent optical and electrical properties.[1,2] While most of the work over the past two decades has focused on zero-dimensional (0D) colloidal quantum dots [QDs, or nanocrystals (NCs)], one-dimensional (1D) systems such as nanowires (NWs) have recently attracted considerable attention due to their unique band and/or ballistic charge transport capabilities,[3] dielectric contrast effects,[4] intrinsic polarization sensitivities,[5,6] and other interesting 1D properties. As a consequence, NWs have numerous applications in nanoscale electronics such as in field effect transistors (FETs),[7] solar cells,[8,9] lasers,[10,11] and sensors for biological applications.[12]

Different synthetic approaches have been developed to make high-quality 1D NWs. They include template-based methods,[13–15] vapor–liquid–solid (VLS) growth,[16–19] supercritical-fluid—liquid–solid (SFLS) growth,[20] and solution—liquid–solid (SLS) growth.[21,22] While most high-quality NWs have been VLS-based, solution approaches offer appealing properties worth investigating. For example, in the SLS technique, growth temperatures generally fall below 400 °C.[23,24] In addition, common growth solvents as well as precursors are used. By exploiting well-known metal–ligand stability constants, improved control over the nucleation and subsequent growth of NWs can be achieved.

In this report we describe the solution-phase synthesis of emissive CdS nanowires. The optical properties of the wires are subsequently investigated at the band edge. Modest emission quantum yields (QYs, 0.05–1%) are observed with unexpectedly long lifetimes that exceed tens of nanoseconds. Complementary transient differential absorption studies reveal relatively fast

*Address correspondence to mkuno@nd.edu.

Received for review October 2, 2007 and accepted January 20, 2008.

**Published online February 9, 2008.**
10.1021/nn700270a CCC: $40.75

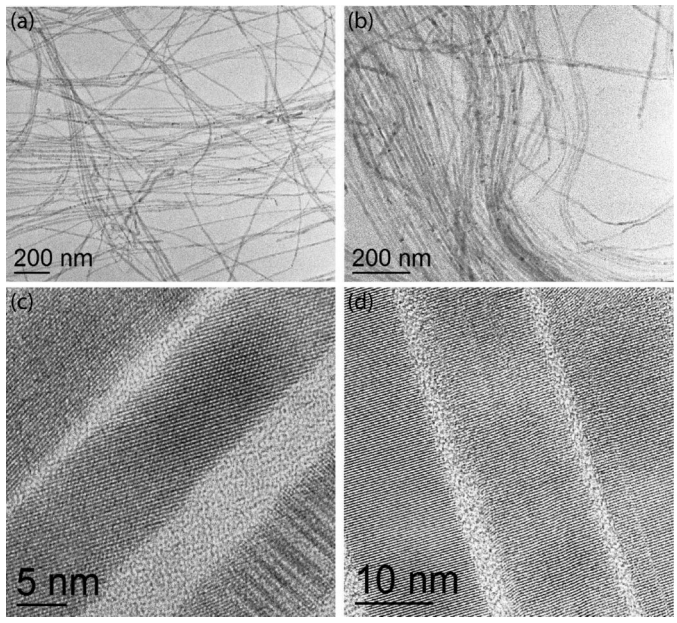


**Figure 1. (a,b) Low- and (c,d) high-resolution TEM images of CdS NWs.**

(300–400 fs) intraband relaxation time scales as well unexpected intensity-dependent transient broadening which appears to stem from band-filling at high carrier densities.

## RESULTS AND DISCUSSION

Relatively little is known about the fundamental optical properties of NWs, despite a handful of preliminary studies.[5,6,25–35] Previous investigations have shown the emergence of intrinsic polarization anisotropies in lithographically defined quantum wires due to the onset of band mixing.[5] Likewise, dielectric contrast effects between NWs and their local environment give rise to polarization anisotropies.[6] Optical disorder has also been seen due to compositional or structural fluctuations.[26] Furthermore, recent ensemble and single NW investigations on CdSe NWs have shown unusual behavior, including intensity-dependent carrier relaxation dynamics[31] as well as unexpected intrawire optical heterogeneities.[25] The latter includes the recent observation of the spatial and intensity modulation of single NW emission using external electric fields.[32] The current study thus adds to a growing body of knowledge about NW carrier physics, focusing on their high carrier density band edge dynamics.

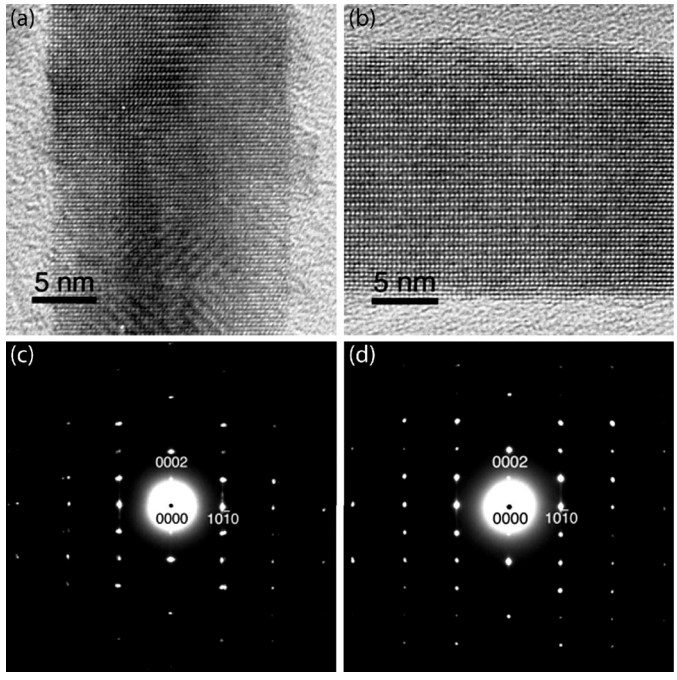


**Figure 2. HRTEM images of wires growing along (a) [0001] and (b) [10|$$10]. (c,d) Corresponding SADPs of the wires. The zone axis is [|$$12|$$10] in both patterns, which are correctly oriented with respect to the images.**

**TABLE 1. Possible Low-Index Zone Axes for Wurtzite NWs with $g$ = 0002 and $g$ = 10|$$10 Growth Directions**

| growth axis | zone axis | $g$ axis |
|---|---|---|
| [0001] | [|$$12|$$10] | 0002 |
| [0001] | [01|$$10] | 0002 |
| [10|$$10] | [|$$12|$$10] | 10|$$10 |
| [10|$$10] | [|$$12|$$11] | 10|$$10 |
| [10|$$10] | [|$$24|$$23] | 10|$$10 |
| [10|$$10] | [0001] | 10|$$10 |

**Materials Characterization.** Figure 1 shows representative low- and high-resolution TEM micrographs of the investigated CdS NWs (additional micrographs are presented in the Supporting Information). On the basis of the images, it is apparent that the wires are crystalline despite their low growth temperature. The average NW diameter is ~14 nm. Ensemble diameter distributions are on the order of ~13% and are similar to, though somewhat smaller than, the initial size distribution of employed Au/Bi NPs (~18%).[24] Corresponding ~5% intrawire diameter variations are seen on the basis of measurements of the wire diameter at 6–7 points along their length. Sizing and inter/intrawire distributions are obtained by examining over 100 NWs. More details about the synthesis, additional descriptions of the parameter space explored, and an ensemble energy-dispersive X-ray spectrum of a NW ensemble can be found in the Supporting Information.

Evidence for both W [0001] and [10|$$10] growth directions is apparent in Figure 2 through HRTEM images (Figure 2a,b) along with corresponding selected area diffraction patterns (SADPs) (Figure 2c,d). Both reveal wires viewed along the [|$$12|$$10] zone axis, with growth directions along the reciprocal lattice vectors $g$ = 0002 and $g$ =10|$$10. (The crystal directions [0001] and [10|$$10] are in the same directions as the corresponding reciprocal lattice vectors.) Table 1 summarizes the possible low-index zone axes for a wurtzite (W) NW with $g$ = 0002 and $g$ =10|$$10. Notably, examples of SADPs with each of the zone axes listed have been observed.

Evidence of the zincblende (ZB) phase has not been observed, despite the small energy difference between

**TABLE 2. Wurtzite XRD Lines Containing Contributions from [0001] and [10|$$10] Oriented NWs**

| growth axis | X-ray lines |
|---|---|
| [0001] | (10|$$10), (11|$$20), (20|$$20), (21|$$30), (30|$$30) |
| [10|$$10] | (0002), (11|$$20), (11|$$22), (11|$$24), |

CdS's ZB and W phases,[36] which might introduce phase admixtures as previously seen in other NWs.[37–40] Although the [01|$$10] W patterns are indistinguishable from [112] ZB patterns, we have not observed either diffraction patterns or HRTEM images of NWs possessing a ZB [110] zone axis. Furthermore, X-ray diffraction (XRD) patterns obtained from CdS samples have reflections which can be assigned exclusively to W reflections. Figure 3 shows the observed XRD pattern from a straight CdS NW ensemble and the corresponding bulk ZB/W JCPDS powder diffraction data (ZB, JCPDS 42-1411; W, JCPDS 77-2306). The experimental pattern contains lines which match the (10|$$10), (0002), (10|$$11), (11|$$20), (10|$$13), (11|$$22), (21|$$30), (21|$$31), and (30|$$30) W lines.

Differences in peak intensities are observed due to the existence of crystallographic texture.[41] Specifically, in an X-ray powder diffractometer, the angles of incidence and reflection from the specimen surface are equal. As a consequence, only crystal planes (*hkl*) parallel to the surface produce observable diffraction lines. NWs lying parallel to the XRD specimen surface therefore contribute only to XRD lines whose crystal planes are parallel to the growth axis and thus to the specimen surface. Wurtzite XRD lines to which NWs with [0001] and [10|$$10] growth axes contribute are listed in Table 2 in order of increasing 2θ.

Comparison with Figure 3 shows that this accounts for all of the strong lines in the experimental pattern, with the exception of (10|$$11), which must also be a W line since it cannot be matched to any ZB line. This suggests the existence of another W growth axis. However, evidence for this has not been seen in current TEM or SADP measurements. In principle, a NW with a [|$$12|$$10] growth axis has (10|$$11) parallel to the wire and could produce the observed (10|$$11) XRD line. Such wires could then be viewed along the [10|$$10] or [0001] zone axes in the TEM with growth along $g$ = |$$12|$$10. Attempts to find such examples have so far been unsuccessful.

It should be noted that lines matching the W (0002), (11|$$20), (11|$$22), (21|$$31), and (30|$$30) lines also match the ZB (111), (220), (311), (331), and (422) lines. However, of these reflections, only the ZB (220) and (422) lines are consistent with the [111] growth axis typical of III−V or II−VI nanowires.[37–39] Thus, taken together with the lack of TEM evidence for ZB NWs, this indicates that (as-made) CdS wires contain only the W phase. Finally, the [10|$$10] growth direction bisects one of the equilateral triangles in the basal plane. Although we are not aware of prior observations of this growth direction in W NWs, it is related to observations in ref 40 of Si/Ge NW growth along [112], since this direction also lies along the bisector of an equilateral triangle in a close-packed {111} plane. Additional HRTEM images of nanowire growth along [10|$$10] are shown in the Supporting Information.

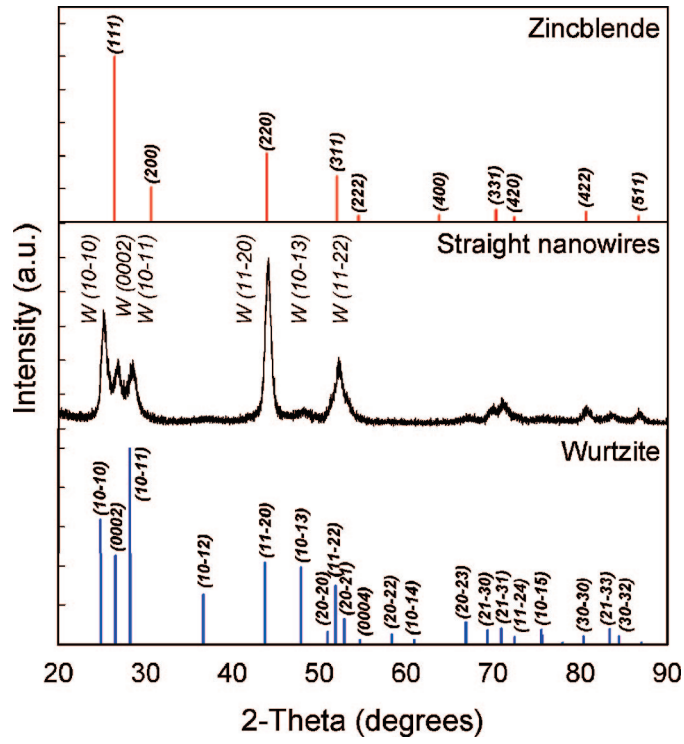


**Figure 3. X-ray diffraction powder patterns of straight CdS NWs. Powder patterns from isotropically oriented samples are shown for comparison (ZB, JCPDS 42-1411; W, JCPDS 77-2306).**

**Optical Properties.** Figure 4a shows the linear absorption spectrum of an ensemble of CdS NWs. Although spectrally broad, an absorption peak close to 480 nm (2.58 eV) is seen, accompanied by apparent gap states farther to the red. No confinement effects are expected because experimental NW diameters are ~14 nm and are generally larger than twice the bulk exciton Bohr radius of CdS ($a_B$ = 2.9 nm). As a consequence, the absorption edge should be close to the bulk band gap [2.4 eV (~517 nm)] with little or no blue-shift.

In addition, complementary band edge emission is seen. As illustrated in Figure 4a, a peak occurs around 490 nm (2.53 eV). The origin of this emission is NW related, as demonstrated by (room-temperature) photoluminescence excitation experiments of the same ensemble (Figure 4b). Specifically, by monitoring the emission at several locations along the red edge of the emission (vertical lines and asterisks, Figure 4) and scanning the excitation to the blue, a spectrum with a profile in qualitative agreement with the linear absorption is obtained. Any potential QD contributions to the emission are excluded through control experiments which

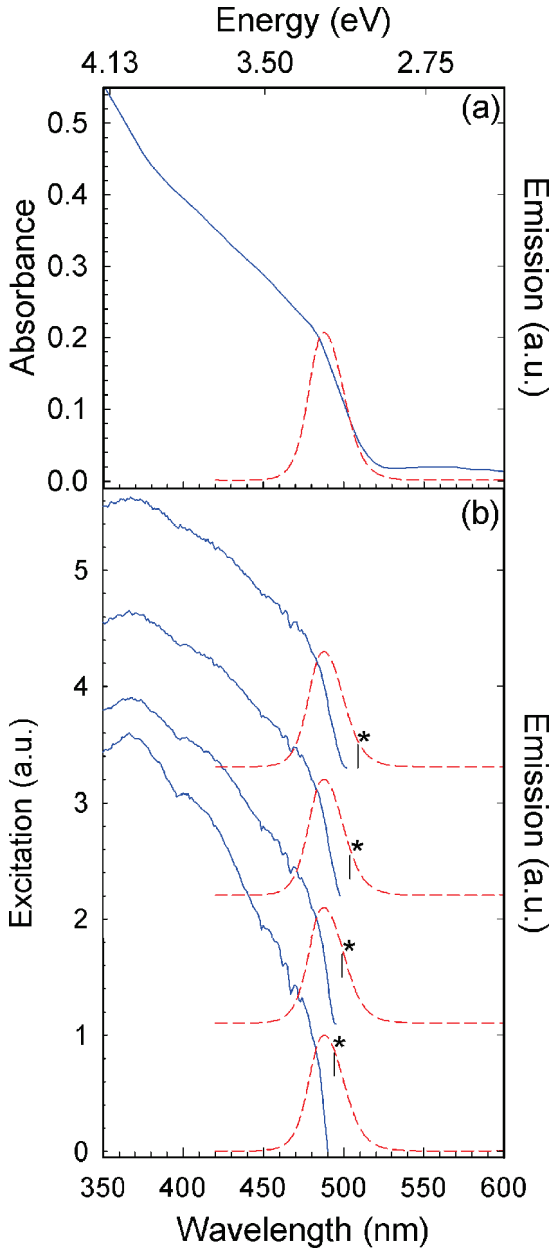


**Figure 4. (a) Linear absorption (solid blue line) and complementary band edge emission (dashed red line) of a CdS NW ensemble. (b) Excitation spectra of the same sample acquired at different spectral locations denoted by asterisks and vertical lines.**

produce NCs under identical conditions and whose emission is centered around 450 nm (2.76 eV).

NW emission, as opposed to QD luminescence, is further confirmed by polarization anisotropy measurements conducted on single wires. Such studies are carried out by exciting individual specimens with 405 nm (3.06 eV) light using a single-molecule imaging microscope. Representative data are shown in Figure 5, where sequential images of a wire at different orientations relative to the excitation polarization are shown. By monitoring the polarization-dependent intensity at a given location along the NW length, a clear modulation of the emission intensity is seen. This is illustrated

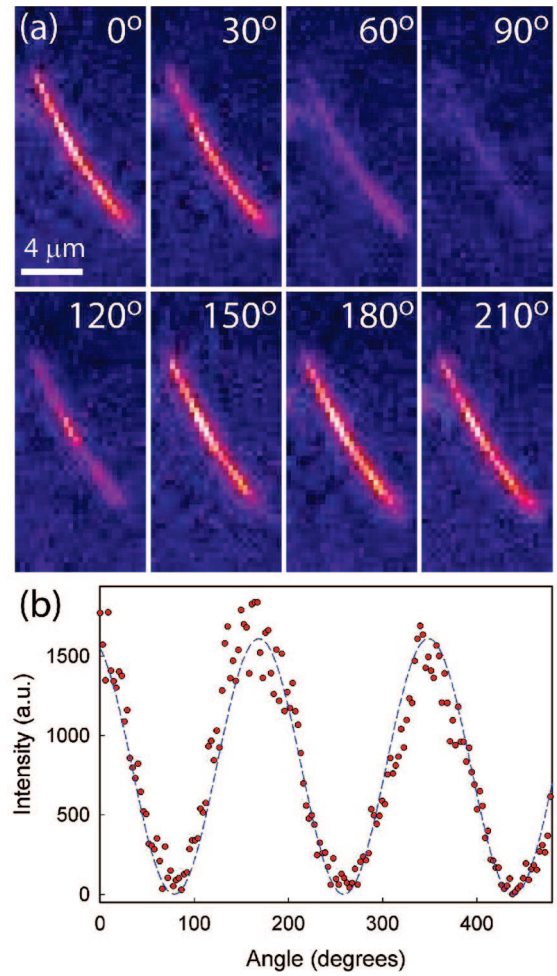


**Figure 5. (a) Sequential images of a single CdS NW as the incident excitation polarization is rotated. (b) Emission intensity modulation at a given position along the NW length. The dashed line is a $\cos^2\theta$ fit to the data, where $\theta$ is the angle between the incident light polarization and the NW axis.**

in Figure 5b, where fits to a $\cos^2\theta$ function yield absorption polarization anisotropies of $\rho = 0.76$ ($\sigma = 0.06$). The results are in good agreement with previously reported $\rho$ values from single CdSe NWs ($\rho = 0.7$–$0.8$).[30]

An estimate of the NW emission QY can be made at this point. In the absence of direct experimental values for CdS NW absorption cross sections ($\sigma$), an expression previously used for both NWs and QDs can be employed to evaluate $\sigma$ far from the band edge (Supporting Information).[25,29] A value for the cross section at 405 nm for a nominal 14 nm diameter, 1 μm long wire is thus obtained: $\sigma_{405nm} = 3.33 \times 10^{-11}$ cm$^2$. A similar value of $\sigma_{387nm} = 3.92 \times 10^{-11}$ cm$^2$ is found at 387 nm and will be relevant for transient differential absorption experiments described below. The emission intensity of individual CdS NWs can then be compared to those of single CdSe wires whose estimated QY is 0.1%.[25] When such intensities are scaled for differences in calculated CdS and CdSe cross sections at 405 nm, CdS QYs of ~0.043% are obtained.

This estimate is corroborated by more direct ensemble QY measurements. In particular, the emission from CdS wires was compared to that of coumarin 343 in ethanol (63% QY). Absorbances were normalized at the excitation wavelength, and areas beneath each emission spectrum were compared. Resulting NW QYs ranged from 0.068 to 0.95%, with the lower limit in good agreement with values obtained from the above single NW measurements. In either case, the actual cause of low quantum yields is not known and may stem from surface defects acting as sources for nonradiative decay.

Complementary ensemble emission lifetime measurements show strong multiexponential decays. The origin of this behavior is not known but may stem from disorder at the band edge, as described below. Traces can generally be fit to three or four exponentials, with a representative plot provided in the Supporting Information. Although short (~100 ps) time scale contributions exist, the majority of the decay occurs over much longer periods, exceeding 10 ns. Average lifetimes from weighted contributions of each component range from 12 to 200 ns. When combined with the above QY measurements, nominal radiative ($\tau_r$) and nonradiative ($\tau_{nr}$) lifetimes are in the microsecond and nanosecond ranges [$\tau_r$(min) = 1.3 μs, $\tau_r$(max) = 394 μs; $\tau_{nr}$(min) = 12 ns, $\tau_{nr}$(max) = 215 ns]. The actual origin of these long lifetimes is not known and requires further investigation.

Complementary transient absorption spectra of CdS NWs were recorded using a commercial femtosecond transient absorption spectrometer. Samples were excited at 387 nm (3.20 eV), followed by a lower intensity, delayed white light probe (420–800 nm; 1.5–2.9 eV). Typical pump intensities ranged from 19 to 433 μJ/cm$^2$ (~$10^{12}$–$10^{13}$ W/m$^2$). Variable delays between 150 fs and 1.5 ns were used to observe carrier relaxation dynamics within the wires. Figure 6 shows representative spectra of the band edge transient at different delays. An apparent bleach at ~482 nm is seen, in good agreement with the spectral position of the linear absorption edge (Figure 6a).

This transient grows in quickly, illustrating rapid intraband carrier relaxation within the wires. Figure 7a shows the evolution of the bleach at different delays immediately after excitation. At short times, an induced absorption is seen on the red edge of the spectrum (~515 nm), possibly Stark-related due to the interaction between pump-induced carriers and electron–hole pairs generated by the probe.[42] This induced absorption quickly decreases in tandem with a gradual redshift and saturation of the bleach. The transient persists for up to ~10 ps (Figure 7b) before decaying due to Auger and other recombination pathways (described below). Estimates for intraband relaxation time scales, obtained from exponential growth fits to the data, range from 300 to 400 fs.

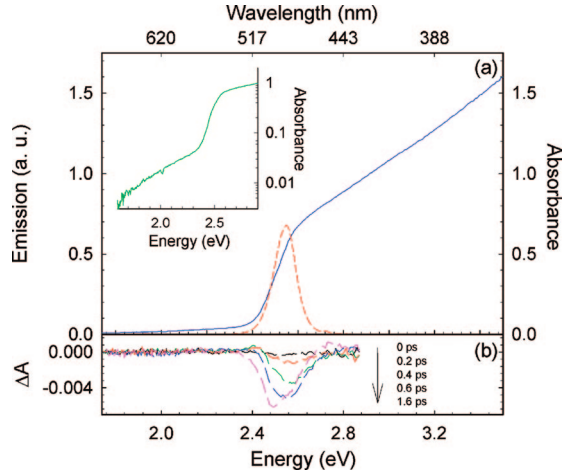


**Figure 6. (a) Linear absorption (solid blue line) and corresponding band edge emission (dashed red line) from an ensemble of CdS NWs. The inset reveals a semilogarithmic plot of apparent band edge tail states. (b) Corresponding transient differential absorption spectra at different delays.**

Subsequent recovery of the band edge bleach occurs over much longer times. Figure 8a shows that observed decays are intensity-dependent, with shorter lifetimes at higher pump fluences. All decays are strongly multiexponential. However, at high pump fluences (>382 μJ/cm$^2$), they can be fit to third-order ki-

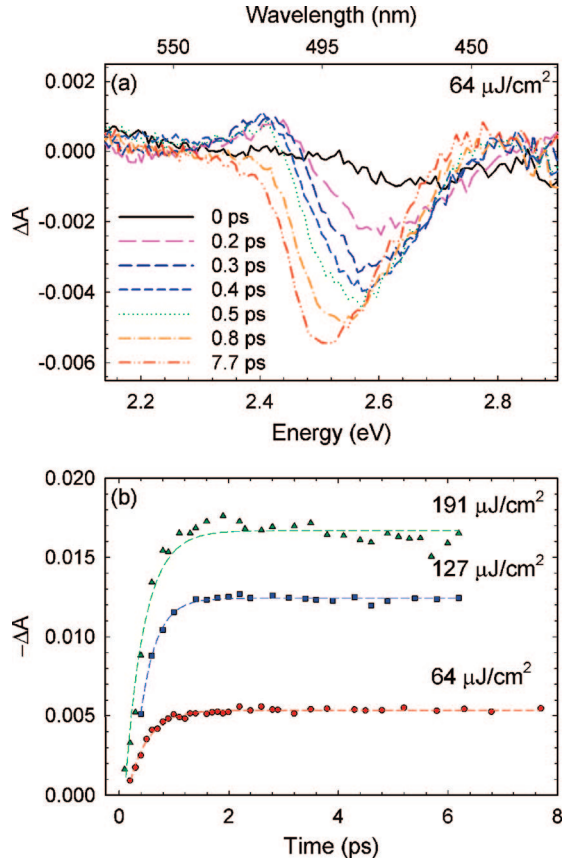


**Figure 7. (a) Spectral dependence of the band edge transient growth. (b) Band edge growth kinetics monitored at the bleach maximum upon saturation.**

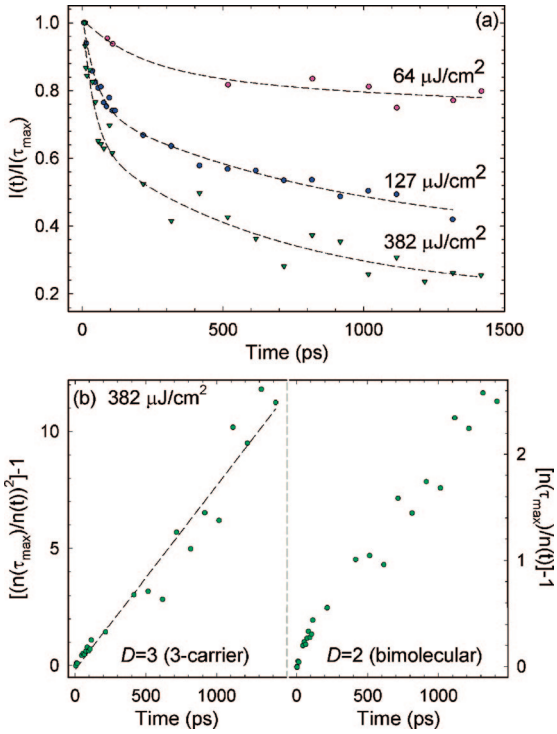


**Figure 8. (a) Intensity-dependent band edge transient decay. (b) Fits to a three-carrier and bimolecular (exciton–exciton annihilation) Auger decay.**

netics, consistent with the Auger relaxation of electrons and holes.

In this respect, the Auger recombination of carriers is an important relaxation pathway in nanostructures at high carrier densities.[42] For example, in colloidal QDs, three-carrier Auger processes are commonly seen due to strong Coulomb interactions between spatially localized electrons and holes. Likewise, in NWs experiencing apparent dielectric contrast effects, bimolecular (exciton–exciton annihilation) kinetics are also observed due to interactions between 1D excitons.[31] In the current experiment, both Auger processes are considered since *a priori* it is not know which will dominate. This is because CdS wires in the present study are not expected to exhibit confinement effects. Being bulk-like, they may therefore exhibit three-carrier (third-order) Auger kinetics. However, dielectric contrast effects could counteract this trend by increasing the electron–hole binding energy, causing the appearance of 1D excitons and, in turn, inducing bimolecular (second-order) kinetics.

In either scenario, Auger decays are described by

$$\frac{dn}{dt} = -C_D n^D \qquad (1)$$

where $n$ is the time-dependent photogenerated carrier density (number/cm$^3$) and $D$ is the order of the decay ($D$ = 2 or 3). Initial photogenerated carrier densities, $n(0)$, are estimated from $n(0) = (\sigma_{387nm} I/h\nu)\tau_p$, where $\sigma_{387nm}$ is the NW cross section (cm$^2$) at 387 nm, $I$ is the incident laser intensity (W/cm$^2$), $h\nu$ is the energy per photon ($J$), and $\tau_p$ is the laser pulse width (150 fs). Resulting $n(0)$ values range from $10^{19}$ to $10^{21}$ cm$^{-3}$, assuming unity carrier generation efficiencies ($\varphi$ = 1). The general solution to eq 1,

$$n(t) = \frac{n(0)}{[1 + (D-1)C_D t n(0)^{D-1}]^{1/(D-1)}} \qquad (2)$$

leads to the following particular solutions for $D$ = 2 and $D$ = 3:

$$\left[\frac{n(0)}{n(t)} - 1\right] = C_2 n(0) t \qquad (D=2) \qquad (3)$$

$$\left[\left(\frac{n(0)}{n(t)}\right)^2 - 1\right] = 2C_3 n(0)^2 t \qquad (D=3) \qquad (4)$$

When plotted against time, both yield linear plots. Data at high pump fluences (382 μJ/cm$^2$), analyzed in this manner, are shown in Figure 8b. The linearity of the leftmost graph suggests that the high-intensity decay is best described by a three-carrier Auger process. By contrast, apparent curvature is seen in the bimolecular fit on the right. An estimate for the Auger constant, $C_3 \approx 10^{-31}$ cm$^6$ s$^{-1}$, extracted from the slope of the three-carrier fit, is in reasonable agreement with previously observed CdSe QD $C_3$ coefficients ($C_3 \approx 10^{-29}$–$10^{-30}$ cm$^6$ s$^{-1}$).[43]

At low pump fluences, neither three-carrier nor bimolecular Auger kinetics describe the band edge decay. Instead, significant curvature is seen in both plots (Supporting Information). This deviation likely stems from the increasing importance of radiative, surface-mediated, and other recombination processes at low carrier densities. In agreement with emission lifetime measurements, the band edge transient becomes long-lived at the lowest pump fluence and shows significant bleaches that extend beyond the 1.5 ns (maximum) delay of the transient absorption spectrometer (Figure 8a, top).

One of the most interesting observations to arise from these studies is an apparent intensity-dependent broadening of the band edge transient. This is illustrated in Figure 9a, where the band edge bleach at saturation is plotted for various pump fluences. From the graph, it is apparent that the bleach blue-shifts and broadens with increasing laser intensity. Both the magnitude of the shift and the spectral broadening are quantified by fits to a Gaussian using a Levenberg–Marquardt nonlinear least-squares algorithm. Extracted peak energies are plotted in Figure 9b for all intensities, along with their corresponding spectral widths in Figure 9c. Over the range of pump fluences studied, clear ~150 meV blue-shifts are seen in the former, while slightly smaller ~100 meV increases appear in the latter.

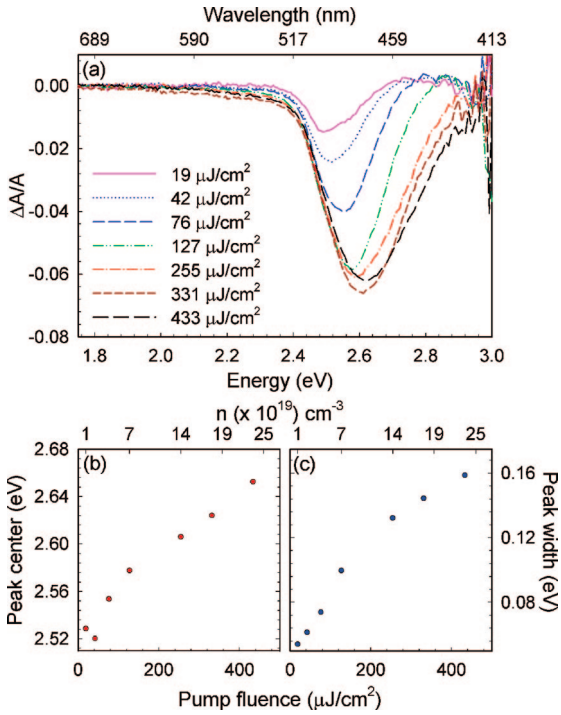


**Figure 9. (a) Intensity-dependent spectral profile of the band edge transient. (b) Intensity-dependent peak energy of the bleach. (c) Associated intensity-dependent spectral width.**

Such behavior has previously been seen in CdS QDs, where blue-shifts and broadening of the band edge transient (or absorption) were observed upon irradiating samples.[44–46] The effect has been attributed to various causes, including band-filling (*i.e.*, a dynamic Burstein–Moss effect),[44] many-body effects,[45] and increased electron–hole pair energies due to surface-trapped carriers.[46] Irrespective of the actual cause, the observation of such prominent spectral broadening effects here likely stems from long carrier lifetimes seen in the above emission lifetime and transient differential absorption measurements.

In general, carrier density-dependent spectral changes in semiconductor absorption/emission contain various contributions.[47] At high densities, band gap renormalization is observed due to exchange-correlation effects. This causes a decrease in the effective band gap, which induces a general red-shift of the absorption. At the same time, many-body effects take place, counteracting this trend. Specifically, screening of excitons by electrons and holes (resulting from the ionization of other excitons) causes a decrease of the exciton binding energy. Exciton–exciton van der Waals interactions also lead to an analogous "screening" (*i.e.*, weakening) of the exciton binding energy. These interactions ultimately increase the exciton absorption/recombination frequency and result in a net blue-shift of the transition. Experimentally, low-temperature studies have shown that both effects coexist with an apparent coincidental cancelation, leaving the spectral center of the absorption (or emission) more or less unchanged.[48] However, significant power-dependent broadening is generally observed on either side of the transition.

While such effects could play a role in explaining observed intensity-dependent spectral changes, several observations argue against this. Namely, an apparent red-shift of the emission with pump fluence is absent. In fact, only a strong blue-shift is seen. Furthermore, experiments are conducted at room temperature on wires with diameters beyond the nominal confinement regime of CdS. As a consequence, ionization of the exciton should be efficient, given modest values of the bulk binding energy (~28 meV).[49] Although dielectric contrast effects could increase this value to energies in excess of 100 meV,[4] no dramatic red-shifts are observed in the linear absorption. Finally, apparent three-carrier Auger recoveries are seen at high carrier densities (Figure 8b), supporting the presence of substantial free carrier populations.

As a consequence, carrier band-filling in both the conduction and valence bands is suggested as the root cause of observed spectral blue-shifts and line broadening. The effect has been explored by considering a simple bulk density-of-states argument. For simplicity, we ignore band gap renormalization, which red-shifts any obtained results. In the model, absorbed photons create electron–hole pairs which undergo rapid intraband relaxation. Both electrons and holes then establish quasi-equilibrium within the NW conduction/valence band. Their respective, quasi-Fermi levels [$\mu_{e(h)}$] are determined by equating the density-of-states-determined concentration of photogenerated electrons (holes) [$n_{e(h)}$] to the initial photogenerated carrier density $n(0)$ through

$$n(0) = n_{e(h)} = \frac{1}{2\pi^2}\left(\frac{2m_{e(h)}kT}{\hbar^2}\right)^{3/2}\int_0^{\infty}\frac{\sqrt{x}\,e^{\mu_{e(h)}-x}}{1+e^{\mu_{e(h)}-x}}\,dx \quad (5)$$

In the expression, electron/hole effective masses of $m_e = 0.2m_0$ and $m_h = 0.8m_0$ are assumed,[44] where $m_0$ is the free electron mass. The last integral is the Fermi−Dirac integral, $F_{1/2}(\mu_{e(h)})$, expressed to make numerical evaluations more convenient. Equation 5 is subsequently solved to extract values of $\mu_{e(h)}$ where we assume $n_e = n_h$ since all excess carriers are photogenerated.

Obtained quasi-Fermi levels then yield associated Fermi−Dirac distributions for carriers in either band,

$$f_{e(h)} = \frac{1}{1+e^{(\Delta E_{e(h)}-\mu_{e(h)}kT)/kT}}$$

For convenience, we assume parabolic conduction and valence bands to determine relevant *excess* electron or hole energies, $\Delta E_{e(h)}$, through

$$\Delta E_{e(h)} = (E_{h\nu} - E_g)\left(\frac{1}{1+m_{e(h)}/m_{h(e)}}\right) \quad (6)$$

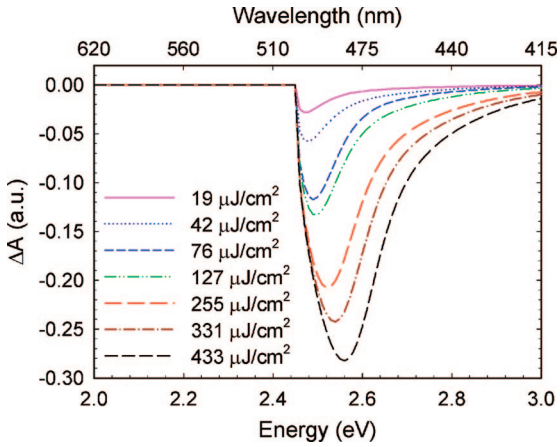


**Figure 10. Qualitative behavior of a density-of-states band-filling model that illustrates blue-shifts and line broadening with increasing carrier density.**

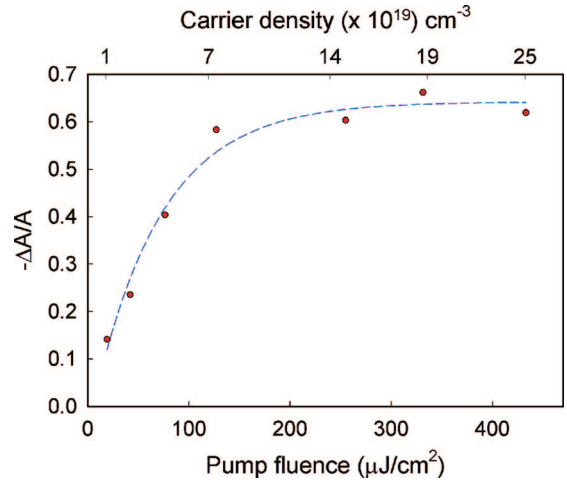


**Figure 11. Intensity-dependent saturation of the band edge transient. The dashed line is a guide to the eye.**

In the expression, $E_{h\nu}$ is the incident photon energy and $E_g$ is the effective band gap of the material. Since the latter value is not known *a priori*, the ensemble absorption spectrum shown in Figure 6 is compared to the general square root dependence of the bulk absorption coefficient to extract a nominal value for $E_g$ (Supporting Information). The comparison yields a value of $E_g \approx 2.45$ eV, in good agreement with the known bulk band gap of CdS (~2.4 eV).

With this, the transient differential absorption can be modeled as a difference spectrum of the form

$$\Delta A = -A\sqrt{E_{h\nu} - E_g}(f_e + f_h - f_e f_h) \qquad (7)$$

where $A$ is a proportionality constant. Results of the model are shown in Figure 10, where it is apparent that it qualitatively reproduces trends seen in the experimental data, namely a progressive blue-shift of the bleach maximum as well as a broadening of the line width with increasing carrier density.

More quantitative comparisons to actual data, however, are complicated by several issues. Specifically, if a unity quantum efficiency for carrier generation ($\varphi = 1$) is assumed, predicted spectral blue-shifts and line widths are much too large. Instead, carrier densities smaller by 1 order of magnitude yield shifts and line widths in good agreement with the data. Predicted peak blue-shifts are on the order of ~90 meV, while line width increases are ~130 meV (Figure 10 and Supporting Information). These values compare favorably with the 150 meV (100 meV) blue-shifts (line width increases) seen experimentally.

Suppression of actual carrier densities in the wires can be rationalized by the rapid population of tail states within the gap (Figure 6, inset). This could then lead to noticeably smaller values of the carrier density. In this respect, a nominal surface-state trap density of $\sim 10^{13}$ $cm^{-2}$ readily explains an order of magnitude decrease in $n(0)$. The existence of such states is apparent in Figure 6 and is also reflected in the failure of the model to accurately describe the low-energy tail of the band edge transient (*i.e.*, the model predicts a square root dependence, whereas the data indicate an exponential decay into the gap). Alternatively, the calculated linear cross section for NWs, $\sigma_{387nm}$, is no longer valid at higher carrier densities, which would then lead to an overestimate of both blue-shifts and spectral line widths.

Another issue preventing a more quantitative comparison between model and experiment is the uncertainty over the actual electron/hole temperature in either band at quasi-equilibrium. Lacking additional information, we assume $T = 300$ K, which is a lower limit. However, despite this quantitative uncertainty, the band-filling model appears to capture the essential physics of the phenomenon, namely the blue-shift and spectral broadening of the band edge transient with increasing carrier density.

In light of long carrier lifetimes and the possibility of gain, the fractional absorbance change ($\Delta A/A$) at the band edge was examined. Results from this analysis are shown in Figure 11, where $\Delta A/A$ has been plotted against pump fluence. From the graph, it is clear that the band edge transition saturates near $\Delta A/A \approx 0.6$. Although no gain is seen, the behavior is in qualitative agreement with the above density-of-states model, which predicts a saturation of $\Delta A/A$ near unity. In this case, the apparent deviation between model and experiment lends support to the involvement of tail states in suppressing $n(0)$, since any change in carrier density due to $\sigma$ variations would still predict unity saturation of $\Delta A/A$. State-filling of band edge states as well as local tail states, enabled in both cases by long carrier lifetimes, is therefore suggested as the root cause of unexpected nonlinearities in the absorption of solution-based CdS NWs.

## SUMMARY

CdS NWs have been synthesized using a seeded solution-based approach. Resulting NW diameters are ~14 nm, with lengths readily exceeding 1 μm. High-resolution TEM micrographs show their high quality/crystallinity and demonstrate that they have the W structure, with growth along [0001] and [10|$$10]. The optical properties of the wires have been studied, with an emphasis on carrier dynamics at the band edge. Unexpectedly long carrier lifetimes, with values exceeding tens of nanoseconds, are observed in both time-resolved emission and transient differential absorption experiments. The latter also reveals an intensity-dependent broadening of the band edge transient, likely associated with these long carrier lifetimes. On the basis of an analysis of intensity-dependent changes in the spectral position as well as line width, band-filling is suggested as the root cause of the effect. This study has relevance to potential applications of NWs and furthers our understanding about the behavior of NWs at high carrier densities.


## EXPERIMENTAL SECTION

**Materials.** The solvents chloroform (≥99.8%), methanol (≥99.8%), and acetone (≥99.5%) were purchased from Fisher Scientific and used as received. To prepare straight CdS wires, trioctylphosphine oxide (TOPO, 99%, Aldrich), dodecylamine (DDA, 98%, Acros), and cadmium oxide (CdO, 99.99+%, Aldrich) were also purchased and used as received. NW growth was carried out in various solvents, such as phenyl ether (99%, Acros), octyl ether (TCI), squalane (99%, Acros), and octadecene (90%, Acros). Solutions of 1 M trioctylphosphine sulfide (TOPS) were prepared by dissolving elemental sulfur in TOP.

Au/Bi core/shell NPs were synthesized according to literature procedures.[24] Briefly, Au NPs were made using a gold biphasic reduction procedure. The resulting particles have diameters of ~1.4 nm, with an estimated 18% size distribution. A bismuth shell is subsequently added by introducing $Bi(Et)_3$ to the Au NPs dispersed in a mild coordinating solvent at 100 °C. Thicker (thinner) shells are achieved by adding more (less) Bi precursor. Typical diameters of the resulting core/shell particles range from 1.4 to 3.0 nm, with a ~20% size distribution. The NP concentration is subsequently "standardized" by matching, to a known value, the absorbance of the solution at 500 nm below (above) any potential Au (Bi) plasmon resonance. An estimate of its concentration is 0.38 mM.[24]

**Synthesis of Nanowires.** A typical synthesis of straight nanowires involves the following: A mixture of TOPO (5 g, 12.9 mmol), CdO (64 mg, 0.5 mmol), DDA (232 mg, 1.25 mmol), and oleic acid (0.8 mL, 2.5 mmol) is heated at 80 °C under vacuum for 1 h. The reaction vessel is then backfilled with nitrogen and heated to 330 °C until the solution is clear. The temperature is then lowered to 290 °C.

An injection solution consisting of "standardized" 1.4 nm diameter (30 μL, 0.184 mmol $Bi(Et)_3$) Au/Bi NPs (200 μL, 76 μmol) and 1 M TOPS (0.5 mL, 0.5 mmol) is prepared inside a glovebox. This solution is then injected into the above reaction mixture. On introduction, the solution color turns orange, and the vessel is allowed to sit at high temperatures for ~2 min.

Once the reaction is complete, the apparatus is allowed to cool. When the temperature falls below 100 °C, toluene is added to prevent TOPO from solidifying. NWs are precipitated from solution by adding an excess of methanol and are separated by centrifuging the suspension. The recovered precipitate is then resuspended in chloroform. Alternatively, the NWs can be "washed" by reprecipitating them with methanol. This process of centrifuging the resulting suspension followed by recovery and resuspension in a solvent is then repeated. The net effect is to reduce the amount of excess surfactant present.

**Instrumentation.** Samples for low- and high-resolution transmission electron microscopy (TEM) analyses were prepared by dropping a dilute solution of CdS NWs in chloroform onto ultrathin carbon-coated copper grids (Ladd). Survey TEMs were conducted during the synthesis of CdS NWs using a JEOL JEM-100SX electron microscope. Additional low- and high-resolution TEM micrographs were taken with a JEOL-2010 instrument.

Ensemble energy-dispersive X-ray spectroscopy (EDXS) samples were prepared by drop-casting wires onto conductive carbon tape and mounting it onto a scanning electron microscope sample holder. EDXS spectra were acquired with a JEOL JXA-8600 super microprobe operating at an accelerating voltage of 15 kV. Wide-angle X-ray diffraction (XRD) specimens were prepared by dropping a chloroform solution of NWs onto an off-cut (0001) quartz substrate and allowing it to dry. XRD scans were taken with a Scintag X-ray diffractometer using Cu Kα (λ = 1.54 Å) radiation.

UV–visible absorption/extinction measurements were conducted using a Cary 50-Bio UV–visible spectrophotometer. Ensemble emission and excitation spectra were acquired with a Spex Fluoromax 3 fluorimeter. Quantum yield experiments involved comparing the NW band edge emission to that of coumarin 343 dissolved in ethanol. Ensemble emission lifetime experiments were carried out with a Jobin Yvon FluoroCube. Transient differential absorption measurements involved a Clark MXR CPA 2010 laser system and an Ultrafast Systems detection package. A fraction of the fundamental was focused onto a sapphire plate to generate a white light continuum. Single NW measurements were performed using a home-built single-molecule imaging instrument described in more detail in ref 25.

*Acknowledgment.* We thank the University of Notre Dame and the Notre Dame Radiation Laboratory for financial support and for use of their facilities. We also thank Kensuke Takechi and Prashant Kamat for access and assistance in using a femtosecond transient absorption spectrometer. M.K. thanks the NSF CAREER (CHE-0547784) and NIRT (ECS-0609249) programs for funding. M.K. is a Cottrell Scholar of Research Corporation.

*Supporting Information Available:* Additional low- and high-resolution TEM micrographs of CdS NWs; further details on the NW synthesis and parameter space explored; energy-dispersive X-ray spectrum of the wires; high-resolution TEM image and accompanying selective area diffraction pattern; absorption cross-section calculation; multiexponential band edge emission decay and fit; Auger three-carrier and bimolecular fits at low pump fluence; comparison of CdS linear absorption to bulk square root energy dependence; and summary of spectral shifts and line width changes from a bulk density of states model. This material is available free of charge *via* the Internet at http://pubs.acs.org.

## REFERENCES AND NOTES


1. Burda, C.; Chen, X.; Narayanan, R.; El-Sayed, M. A. Chemistry and Properties of Nanocrystals of Different Shapes. *Chem. Rev.* **2005**, *105*, 1025–1102.
2. Cozzoli, P. D.; Pellegrino, T.; Manna, L. Synthesis, Properties and Perspectives of Hybrid Nanocrystal Structures. *Chem. Soc. Rev.* **2006**, *35*, 1195–1208.
3. Zhou, X.; Dayeh, S. A.; Aplin, D.; Wang, D.; Yu, E. T. Direct Observation of Ballistic and Drift Carrier Transport Regimes in InAs Nanowires. *Appl. Phys. Lett.* **2006**, *89*, 053113/1–053113/3.
4. Muljarov, E. A.; Zhukov, E. A.; Dneprovskii, V. S.; Masumoto, Y. Dielectrically Enhanced Excitons in Semiconductor-Insulator Quantum Wires: Theory and Experiment. *Phys. Rev. B* **2000**, *62*, 7420–7432.

5. Vouilloz, F.; Oberli, D. Y.; Dupertuis, M. A.; Gustafsson, A.; Reinhardt, F.; Kapon, E. Polarization Anisotropy and Valence Band Mixing in Semiconductor Quantum Wires. *Phys. Rev. Lett.* **1997**, *78*, 1580–1583.
6. Wang, J.; Gudiksen, M. S.; Duan, X.; Cui, Y.; Lieber, C. M. Highly Polarized Photoluminescence and Photodetection from Single Indium Phosphide Nanowires. *Science* **2001**, *293*, 1455–1457.
7. Xiang, J.; Lu, W.; Hu, Y.; Wu, Y.; Yan, H.; Lieber, C. M. Ge/Si Nanowire Heterostructures as High-Performance Field-Effect Transistors. *Nature* **2006**, *441*, 489–493.
8. Law, M.; Greene, L. E.; Johnson, J. C.; Saykally, R.; Yang, P. Nanowire Dye-Sensitized Solar Cells. *Nat. Mater.* **2005**, *4*, 455–459.
9. Baxter, J. B.; Walker, A. M.; van Ommering, K.; Aydil, E. S. Synthesis and Characterization of ZnO Nanowires and Their Integration into Dye-Sensitized Solar Cells. *Nanotechnology* **2006**, *17*, S304–S312.
10. Huang, M. H.; Mao, S.; Feick, H.; Yan, H.; Wu, Y.; Kind, H.; Weber, E.; Russo, R.; Yang, P. Room-Temperature Ultraviolet Nanowire Nanolasers. *Science* **2001**, *292*, 1897–1899.
11. Duan, X.; Huang, Y.; Agarwal, R.; Lieber, C. M. Single-Nanowire Electrically Driven Lasers. *Nature* **2003**, *421*, 241–245.
12. Patolsky, F.; Lieber, C. M. Nanowire Nanosensors. *Mater. Today* **2005**, *8* (4), 20–28.
13. Xu, D.; Chen, D.; Xu, Y.; Shi, X.; Guo, G.; Gui, L.; Tang, Y. Preparation of II−VI Group Semiconductor Nanowire Arrays by DC Electrochemical Deposition in Porous Aluminum Oxide Templates. *Pure Appl. Chem.* **2000**, *72*, 127–135.
14. Lakshmi, B. B.; Dorhout, P. K.; Martin, C. R. Sol−Gel Template Synthesis of Semiconductor Nanostructures. *Chem. Mater.* **1997**, *9*, 857–862.
15. Che, G.; Lakshmi, B. B.; Martin, C. R.; Fisher, E. R. Chemical Vapor Deposition Based Synthesis of Carbon Nanotubes and Nanofibers Using a Template Method. *Chem. Mater.* **1998**, *10*, 260–267.
16. Wagner, R. S.; Ellis, W. C. Vapor−Liquid−Solid Mechanism of Single Crystal Growth. *Appl. Phys. Lett.* **1964**, *4*, 89–90.
17. Yazawa, M.; Koguchi, M.; Hiruma, K. Heteroepitaxial Ultrafine Wire-Like Growth of InAs on GaAs Substrates. *Appl. Phys. Lett.* **1991**, *58*, 1080–1082.
18. Yazawa, M.; Koguchi, M.; Muto, A.; Ozawa, M.; Hiruma, K. Effect of One Monolayer of Surface Gold Atoms on the Epitaxial Growth of InAs Nanowhiskers. *Appl. Phys. Lett.* **1992**, *61*, 2051–2053.
19. Morales, A. M.; Lieber, C. M. A Laser Ablation Method for the Synthesis of Crystalline Semiconductor Nanowires. *Science* **1998**, *279*, 208–211.
20. Holmes, J. D.; Johnston, K. P.; Doty, R. C.; Korgel, B. A. Control of Thickness and Orientation of Solution-Grown Silicon Nanowires. *Science* **2000**, *287*, 1471–1473.
21. Trentler, T.; Hickman, K. M.; Goel, S.; Viano, A. M.; Gibbons, P. C.; Buhro, W. E. Solution−Liquid−Solid Growth of Crystalline II−V Semiconductors: An Analogy to Vapor−Liquid−Solid Growth. *Science* **1995**, *270*, 1791–1794.
22. Wang, F.; Dong, A.; Sun, J.; Tang, R.; Yu, H.; Buhro, W. E. Solution−Liquid−Solid Growth of Semiconductor Nanowires. *Inorg. Chem.* **2006**, *45*, 7511–7521.
23. Buhro, W. E.; Hickman, K. M.; Trentler, T. J. Turning Down the Heat on Semiconductor Growth: Solution-Chemical Syntheses and the Solution−Liquid−Solid Mechanism. *Adv. Mater.* **1996**, *8*, 685–688.
24. Grebinksi, J. W.; Richter, K. L.; Zhang, J.; Kosel, T. H.; Kuno, M. Synthesis and Characterization of Au/Bi Core/Shell Nanocrystals: A Precursor toward II−VI Nanowires. *J. Phys. Chem. B* **2004**, *108*, 9745–9751.
25. Protasenko, V. V.; Hull, K. L.; Kuno, M. Disorder-Induced Optical Heterogeneity in Single CdSe Nanowires. *Adv. Mater.* **2005**, *17*, 2942–2949.
26. (a) Zimmerman, R.; Grobe, F.; Runge, E. Excitons in Semiconductor Nanostructures with Disorder. *Pure Appl. Chem.* **1997**, *69*, 1179–1186. (b) Intonti, F.; Emiliani, V.; Lienau, C.; Elsaesser, T.; Notzel, R.; Ploog, K. H. Low Temperature Near-Field Luminescence Studies of Localized and Delocalized Excitons in Quantum Wires. *J. Microsc.* **2001**, *202*, 193–201.
27. Yu, H.; Loomis, R. A.; Gibbons, P. C.; Wang, L. W.; Buhro, W. E. Cadmium Selenide Quantum Wires and the Transition from 3D to 2D Confinement. *J. Am. Chem. Soc.* **2003**, *125*, 16168–16169.
28. Yu, H.; Li, J.; Loomis, R. A.; Wang, L. W.; Buhro, W. E. Two-Versus Three-Dimensional Quantum Confinement in Indium Phosphide Wires and Dots. *Nat. Mater.* **2003**, *2*, 517–520.
29. Protasenko, V.; Bacinello, D.; Kuno, M. Experimental Determination of the Absorption Cross-Section and Molar Extinction Coefficient of CdSe and CdTe Nanowires. *J. Phys. Chem. B* **2006**, *110*, 25322–25331.
30. Zhou, R.; Chang, H.-C.; Protasenko, V.; Kuno, M.; Kumar, A.; Xing, H.; Jena, D. CdSe Nanowires with Illumination-Enhanced Conductivity: Induced Dipoles, Dielectrophoretic Assembly, and Field-Sensitive Emission. *J. Appl. Phys.* **2007**, *101*, 073704/1–073704/9.
31. Robel, I.; Bunker, B.; Kamat, P. V.; Kuno, M. Exciton Recombination Dynamics in CdSe Nanowires: Bimolecular to Three-Carrier Auger Kinetics. *Nano Lett.* **2006**, *6*, 1344–1349.
32. Protasenko, V. V.; Gordeyev, S.; Kuno, M. Spatial and Intensity Modulation of Nanowire Emission Induced by Mobile Charges. *J. Am. Chem. Soc.* **2007**, *129*, 13160–13171.
33. Hoang, T. B.; Titova, L. B.; Jackson, H. E.; Smith, L. M.; Yarrison-Rice, J. M.; Lensch, J. L.; Lauhon, L. J. Temperature Dependent Photoluminescence of Single CdS Nanowires. *Appl. Phys. Lett.* **2006**, *89*, 123123/1–123123/3.
34. Shan, C. X.; Liu, Z.; Hark, S. K. Photoluminescence Polarization in Individual CdSe Nanowires. *Phys. Rev. B* **2006**, *74*, 153402/1–153402/4.
35. Gudiksen, M. S.; Wang, J. F.; Lieber, C. M. Size-Dependent Photoluminescence from Single Indium Phosphide Nanowires. *J. Phys. Chem. B* **2002**, *106*, 4036–4039.
36. (a) Wei, S.-H.; Zhang, S. B. *Phys. Rev. B* **2000**, *62*, 6944. (b) Yeh, C.-Y.; Lu, Z. W.; Froyen, S.; Zunger, A. Zinc-Blende–Wurtzite Polytypism in Semiconductors. *Phys. Rev. B* **1992**, *46*, 10086–10097.
37. Grebinski, J. W.; Hull, K. L.; Zhang, J.; Kosel, T. H.; Kuno, M. Solution-Based Straight and Branched CdSe Nanowires. *Chem. Mater.* **2004**, *16*, 5260–5272.
38. Kuno, M.; Ahmad, O.; Protasenko, V.; Bacinello, D.; Kosel, T. H. Solution-Based Straight and Branched CdTe Nanowires. *Chem. Mater.* **2006**, *18*, 5722–5732.
39. Hiruma, K.; Yazawa, M.; Katsuyama, T.; Ogawa, K.; Haraguchi, K.; Koguchi, M.; Kakibayashi, H. Growth and Optical Properties of Nanometer-Scale GaAs and InAs Whiskers. *J. Appl. Phys.* **1995**, *77*, 447–462.
40. Davidson, F. M.; Lee, D. C.; Fanfair, D. D.; Korgel, B. A. Lamellar Twinning in Semiconductor Nanowires. *J. Phys. Chem. C* **2007**, *111*, 2929–2935.
41. Hull, K. L.; Grebinski, J. W.; Kosel, T. H.; Kuno, M. Induced Branching in Confined PbSe Nanowires. *Chem. Mater.* **2005**, *17*, 4416–4425.
42. Klimov, V. I. Spectral and Dynamical Properties of Multiexcitons in Semiconductor Nanocrystals. *Annu. Rev. Phys. Chem.* **2007**, *58*, 635–673.
43. Klimov, V. I.; Mikhailovsky, A. A.; McBranch, D. W.; Leatherdale, C. A.; Bawendi, M. G. Quantization of Multiparticle Auger Rates in Semiconductor Quantum Dots. *Science* **2000**, *287*, 1011–1013.
44. Kamat, P. V.; Dimitrijevic, N. M.; Nozik, A. J. Dynamic Burstein−Moss Shift in Semiconductor Colloids. *J. Phys. Chem.* **1989**, *93*, 2873–2875.
45. Hilinski, E. F.; Lucas, P. A.; Wang, Y. A Picosecond Bleaching Study of Quantum-Confined Cadmium Sulfide

Microcrystallites in a Polymer Film. *J. Chem. Phys.* **1988**, *89*, 3435–3431.
46. Henglein, A.; Kumar, A.; Janata, E.; Weller, H. Photochemistry and Radiation Chemistry of Semiconductor Colloids: Reaction of the Hydrated Electron with CdS and Non-linear Optical effects. *Chem. Phys. Lett.* **1986**, *132*, 133–136.
47. (a) Haug, H.; Schmitt-Rink, S. Basic Mechanisms of the Optical Nonlinearities of Semiconductors Near the Band Edge. *J. Opt. Soc. Am. B* **1985**, *2*, 1135–1142. (b) Banyai, L.; Koch, S. W. A Simple Theory for the Effects of Plasma Screening on the Optical Spectra of Highly Excited Semionductors. *Z. Phys. B Condensed Matter* **1986**, *63*, 283–291.
48. (a) Kappei, L.; Szczytko, J.; Morier-Genoud, F.; Deveaud, B. Direct Observation of the Mott Transition in an Optically Excited Semiconductor QuantumWell. *Phys. Rev. Lett.* **2005**, *94*, 147403/1–147403/4. (b) Guillet, T.; Grousson, R.; Voliotis, V.; Menant, M.; Wang, X. L.; Ogura, M. Mott Transition from a Diluted Exciton Gas to a Dense Electron-Hole Plasma in a Single V-shaped Quantum Wire. *Phys. Rev. B* **2003**, *67*, 235324/1–235324/6.
49. *Excitonic Processes in Solids*; Ueda, M., Kanzaki, H., Kobayashi, K., Toyozawa, Y., Hanamura, E., Eds.; Springer Series in Solid State Sciences *60*; Springer Verlag: Berlin, 1986.